Available online at www.sciencedirect.com

jmr&t Journal of Materials Research and Technology

journal homepage: www.elsevier.com/locate/jmrt

Original Article

Microstructure and porosity evolution of alkali activated slag at various heating temperatures

Ikmal Hakem Aziz [a], *Mohd Mustafa Al Bakri Abdullah* [a,*], *M.A.A. Mohd Salleh* [a], *Sorachon Yoriya* [b], *Jitrin Chaiprapa* [c], *Catleya Rojviriya* [c], *Long Yuan Li* [d]

[a] *Center of Excellence Geopolymer and Green Technology, School of Materials Engineering, Universiti Malaysia Perlis (UniMAP), P.O. Box 77, D/A Pejabat Pos Besar, 01000, Kangar, Perlis, Malaysia*

[b] *National Metal and Material Technology Center (MTEC), National Science and Technology Development Agency (NSTDA), 114 Thailand Science Park, Pahonyothin Rd., Khlong 1, Khlong Luang, Pathum Thani, 12120, Thailand*

[c] *Synchrotron Light Research Institute, Muang, Nakhon Ratchasima, 30000, Thailand*

[d] *School of Engineering, University of Plymouth, Plymouth, PL4 8AA, United Kingdom*

ARTICLE INFO

Article history:
Received 26 August 2020
Accepted 14 November 2020
Available online 24 November 2020

Keywords:
Alkali activated slag
Porosity
Crystallisation
Electron backscatter diffraction

ABSTRACT

This paper elucidated the microstructural and porosity evolution of alkali activated slag at 800 °C up to 1200 °C. The microstructural analysis obtained shows the changes in surface densification of glassy phase and nucleation of dynamical grains within the alkali activated slag when in contact with high heating temperature. Using synchrotron radiation X-ray tomographic microscopy, the number of pores in alkali activated slag decreased with increasing heating temperature. The 3D pores distribution also demonstrated significant increase in the range size of ~20 μm with the appearance of isolated and intergranular pores at 1200 °C. These changes also led to the anorthite crystallisation indicated by high angle grain boundaries and preferred crystal orientation. The evolution of porosity and crystalline phase is contributed to the development of internal strain after heating at high temperature environment.

1. Introduction

Over a decade, the utilization of slag in cement and concrete researches based on alkali activation has been studied. Alkali-activation of slag is an alternative material for slag-blended and ordinary Portland cement. Alkali-activated material has outstanding advantageous properties such as better strength development, excellent durability, lower environmental impacts and preferable thermal stability. Frequently, the production of alkali activated slag (AAS) can be formed through chemical reaction of sodium hydroxide, sodium silicate and waste metal precursor slag such as ground granulated blast furnace slag, steel slag and copper slag [1–3].

* Corresponding author.
E-mail addresses: ikmalhakem@gmail.com (I.H. Aziz), mustafa_albakri@unimap.edu.my (M.M.A.B. Abdullah), arifanuar@unimap.edu.my (M.A.A. Mohd Salleh), sorachy@mtec.or.th (S. Yoriya), jitrin@slri.or.th (J. Chaiprapa), catleya@slri.or.th (C. Rojviriya), long-yuan.li@plymouth.ac.uk (L.Y. Li).

https://doi.org/10.1016/j.jmrt.2020.11.041

Table 1 – Composition of ground granulated blast furnace slag obtained by X-ray fluorescence.

Element	wt (%)
Aluminium oxide (Al_2O_3)	10.50
Silicon dioxide (SiO_2)	30.40
Calcium oxide (CaO)	50.37
Magnesium oxide (MgO)	3.20
Iron (III) oxide (Fe_2O_3)	0.53
Phosphorus pentoxide (P_2O_5)	0.04
Sulphur trioxide (SO_3)	0.58
Sodium oxide (Na_2O)	0.28
Potassium oxide (K_2O)	0.32
Titanium dioxide (TiO_2)	0.98
Manganese oxide (MnO)	0.99

Alkali activated slag is an inorganic material that has been discovered displaying excellent performance in thermal stability at high temperature exposure. Referring to the studies by Davidovits [4] the ceramic-properties was emphasized with the formation of several crystalline aluminosilicate phases with high melting point of up to 1000 °C. This physiochemical characteristic obtained is essential to preserve the structural integrity upon heating at high temperatures. Alkali activated slag binder is commonly synthesized in ambient temperature [5,6] and formed in amorphous phase. As heating temperature increases, the evolution of crystalline phase began to appear. In recent studies, the characteristic of concrete at elevated temperature is the major concern while considering the structure durability for high performance application [7,8].

Presently, the research on alkali activated slag at high temperature exposure mainly evaluates on several aspects namely strength properties, physical appearance, microstructural changes and crystallinity behavior [9,10]. Park et al. [11], investigated the physical behavior and chemical property of alkali activated fly ash/slag at high temperature condition. Unconfined compressive test was conducted after exposure to high temperatures on AAS samples. Test results indicated that the crystallisation of the binder gel contributed to porosity phenomena and resulted in strength deformation at temperature above 400 °C. Rovnanik et al. [12], recently prepared the alkali activated slag paste exposed up to temperature of 1200 °C, the strength properties slightly increased although it implies continuous changes in pore distribution and resulted in higher porosity. Moreover, an irregular calcium aluminosilicate structure fills the space between akermanite crystals. However, in contrast with the findings by Burciaga-Diaz et al. [13] reported the crystallisation of alkali activated slag/metakaolin up to 1200 °C traces the formation of calcite, quartz and akermanite which is believed to be the worst performance in terms of strength. Despite the importance of durability characteristic of the material at high temperature condition, pore structure and crystallinity behavior of a heterogenous material also play a key role. The crystalline phase and pore network of alkali activated slag can be obtained using the x-ray diffraction, microtomography, mercury intrusion porosimetry and microstructure [14,15]. However, the major limitation of this conventional technique is inadequate analysis about three-dimensional data and detailed crystallographic, microstructural observation, which is essential to precisely determine the pore network and grain connectivity. Understanding the microstructural evolution of the alkali activated slag at high heating temperature is therefore vitally valuable for cement and concrete materials.

There are some shortcomings of the conventional method of scanning electron microscopy (SEM) which only provides the pore shape assumption and determining phase connectivity information in 2D images [16,17]. Otherwise, highly connected pore network is hard to be obtained for alkali activated slag from the segmented pore if the conventional x-ray tomography (μ-CT) was used [18]. Synchrotron X-ray tomography (SXTM) allows a three-dimensional image of pores and the network arrangement with a high resolution [19]. Electron back scatter diffraction (EBSD) is a technique which has provided a detailed understanding of the crystallography microstructural behavior of polycrystalline material [20]. This advanced technique performed with scanning electron (SEM) was utilized to measure crystal orientation in ceramic fabricated samples [21,22] among other areas of steel [23,24] and electronic materials [25,26], but which has not previously analysed for the alkali activated materials. Furthermore, the details of phase mapping, grain boundary characteristic, grains size, crystallographic texture and strain analysing within the materials are easily obtained using EBSD. The imaging of strain orientation can be applied to distinguish the grains deformation and recrystallisation [27,28].

The aims of this current work are to characterise the pore network and crystallographic microstructural evolution of alkali activated slag at high heating temperature using synchrotron X-ray tomographic microscopy (SXTM) and EBSD technique. Based on these results, the correlation between pore network and crystallography in alkali activated slag at high temperature environments is summarized. The derived observations are correlated with the strain analysis obtained using advanced technique of EBSD.

2. Materials and methods

2.1. *Sample preparation and experimental details*

The samples used in this work was formed by the aluminosilicate source of slag powder (GGBFS; Ann Joo Integrated Steel

Table 2 – Detail of mixture for alkali activated slag.

Samples	GGBFS (kg/m^3)	Na_2SiO_3 solution (kg/m^3)	NaOH solution (kg/m^3)	Solid-to-Liquid ratio (SL)	Alkaline activator ratio	Heating temperature (°C)
A	937.5	223.21	89.3	3.0	2.5	800
B	937.5	223.21	89.3	3.0	2.5	1000
C	937.5	223.21	89.3	3.0	2.5	1200

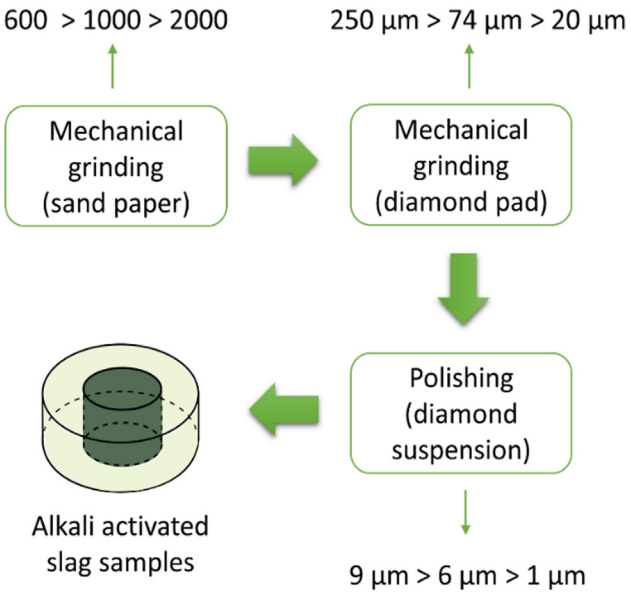

Fig. 1 – Detail of alkali activated slag sample preparation for EBSD technique.

Sdn. Bhd) with the chemical compositions as tabulated in Table 1 (determined by bench top X-ray fluorescence spectrometer; PW4030). The liquid sodium silicate (Na_2SiO_3) used was supplied by South Pacific Chemical Industries Sdn. Bhd., Malaysia consists of 30.1% SiO_2, 9.4% Na_2O and 60.5% H_2O (SiO_2/Na_2O ratio = 3.2). The sodium hydroxide solution was prepared to a concentration of 10M.

The precursor samples used was solely 100% GGBFS activated using solid pellet sodium hydroxide and liquid of sodium silicate, at a solid to liquid ratio (S/L) of 3.0 and alkaline activator ratio (S/N) of 2.5. The selected mixing design was choose based on the optimum compressive strength [29]. The details of the mixture design of the samples are tabulated in Table 2. The precursor slag powder was mixed with alkaline activator solution for 5 min, then being casted into 2.5 mm diameter x 3 mm height cylinders which were sealed to minimize moisture loss and cured at room temperature for 28 days. Three samples were subjected to three different heating temperatures (800 °C, 1000 °C, and 1200 °C) with a heating rate of 10 °C/min and soaking time for 1 h by using standard electrically-heated furnace.

2.2. *Characterisation*

2.2.1. *Microstructural characterisation and chemical bond analysis*

The microstructural changes of heated alkali activated slag was performed by using JSM-6460LA model Scanning Electron Microscope (JOEL) equipped with secondary electron detector and energy-dispersive x-ray spectroscopy. The samples were coated with palladium. The microstructure analysis was carried out at 10 kV acceleration voltage with 10 mm working distance.

Fourier infrared spectroscopy analysis (FTIR) was carried out to identify shifting functional groups of the produced heated alkali activated slag by using PerkinElmer RX1 spectrometer in transmittance mode with a frequency ranged

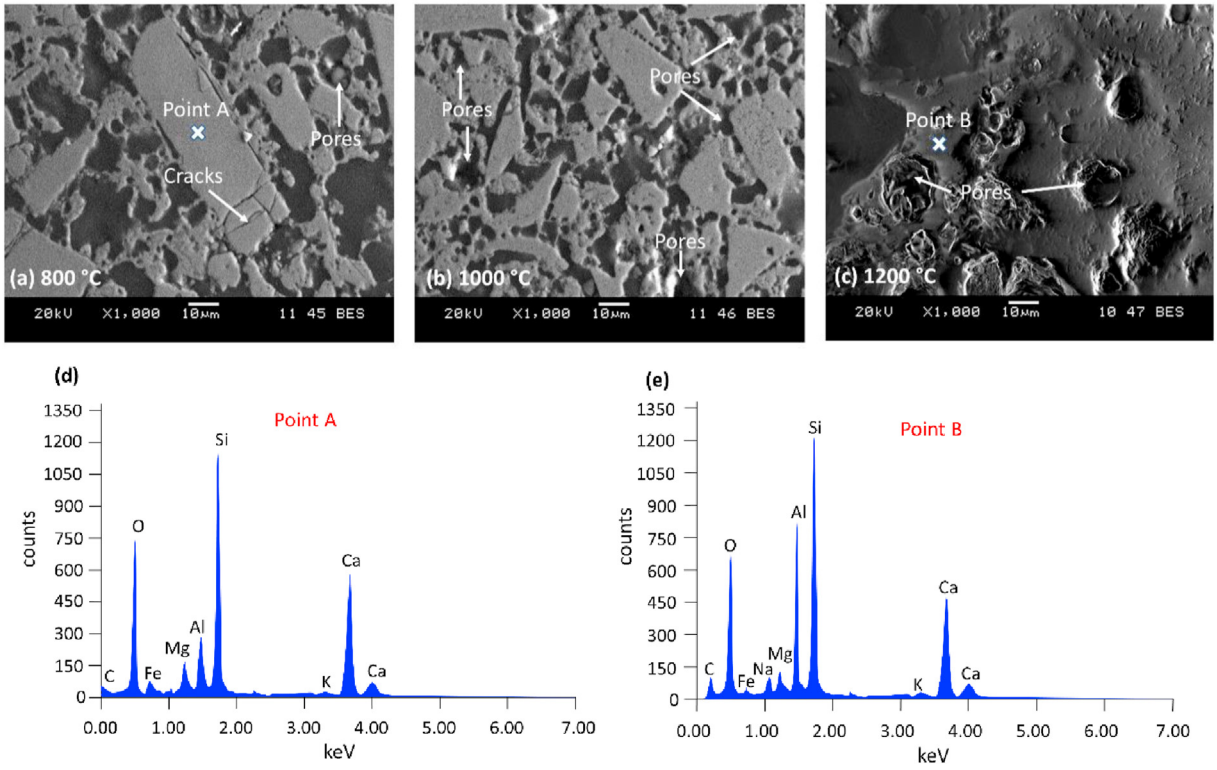

Fig. 2 – Detail SEM-EDS micrograph of grain on alkali activated slag at various heating temperatures (a) 800°C, (b) 1000°C, and (c) 1200°C. Elemental composition of the crystalline (d) gehlenite grain and (e) anorthite grain.

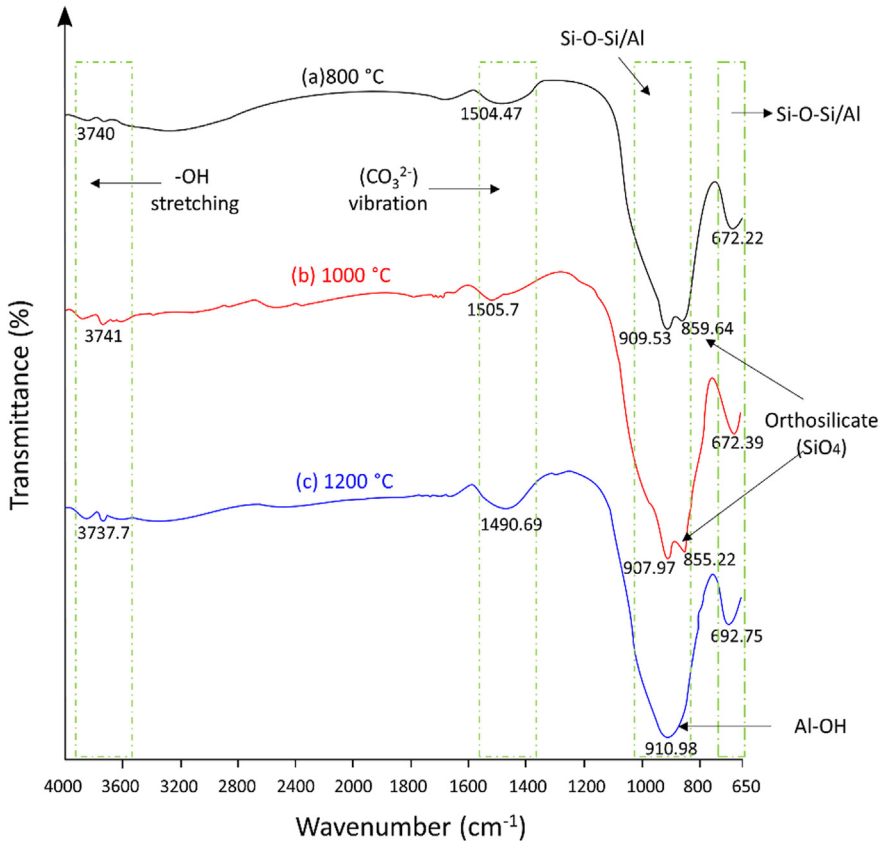

Fig. 3 – IR spectra of alkali activated slag at various heating temperatures.

between 4000 cm^{-1} to 650 cm^{-1} at 4 cm^{-1} resolution. The specimens were evaluated by applying Potassium Bromide (KBr) pellets methodology.

2.2.2. *Synchrotron radiation X-ray tomographic microscopy (SXTM) and micro X-ray fluorescence (μ-XRF)*

The element distribution of heated alkali activated slag was performed by using synchrotron μ-XRF at BL6b beamline at the Synchrotron Light Research Institute (SLRI), Thailand. The size of the white X-ray beam was generated from a bending magnet with the limitation of beam size using a circular aperture and a polycapillary lens to focus (beam size of 30 μm × 30 μm) on the samples [30]. The energy of micro X-ray beam would have been 2–12 keV without monochromator feature. The samples were placed 90° level between the ccd camera and X-ray beam, while the Vortex EM-650 silicon drift detector was used to amass the emitted fluorescent X-ray from the samples. The experiments were performed in helium gas atmosphere and the exposure time for each point was 30 s. A total scan of 2380 points was obtained with a detector time close to 20%. The results were then analysed using the PyMca software [31].

The heated samples of alkali activated slag were used in the current study. Each sample was placed in a cylindrical sample holder filled with cottons soaked in formaldehyde solution to prevent displacement and dehydration during tomographic scanning. SXTM experiments were conducted at the Synchrotron XTM beamline (BL1.2 W: X-ray imaging and tomographic microscopy), Synchrotron Light Research Institute, Thailand. The SXTM imaging of heated alkali activated slag was carried out using filtered polychromatic X-ray beam with a maximum area of 4 × 8 mm^2 at 10 keV, at a distance of 34 m from the source [32]. The sample projections were equipped with 200-μm-thick YAG:Ce scintillator, the white beam microscope (Optique Peter, France) and the pco.edge 5.5 sCMOS camera (2560 × 2160 pixels, 16 bits). The total tomographic scan was obtained at a pixel size 1.44 μm, which provides a field of view (3.1 × 3.7 mm^2). Two scans of reconstruction tomographic volume were performed to determine the fine details of heated alkali activated slag. The first scan was captured over 180° and the other 180° scan was captured on vertical axis of rotation as shifted parallel and horizontally to the actual camera [33]. Afterwards, the X-ray projection were normalized by flat-field correction, stitched, and reconstructed using Octopus software [34]. The 3D images of tomographic volume were rendered using Drishti software.

2.2.3. *Electron backscatter diffraction (EBSD) technique*

The heated alkali activated slag samples were mechanically grounded with a series of SiC papers from 600, 1000 and 2000 grit followed by grounded with diamond pad from 250 μm, 74 μm and 20 μm. Then, the samples were polished using diamond pastes (9 μm, 6 μm and 1 μm). The detail of sample preparation was portrayed in Fig. 1. Microstructural evolutions of the specimens were investigated by EBSD with a Nordlys-II(S) detector attached to HITACHI -SU8230. During the EBSD characterization, the samples were tilted about 70° and operated at 25 kV. A working distance of 24 mm was

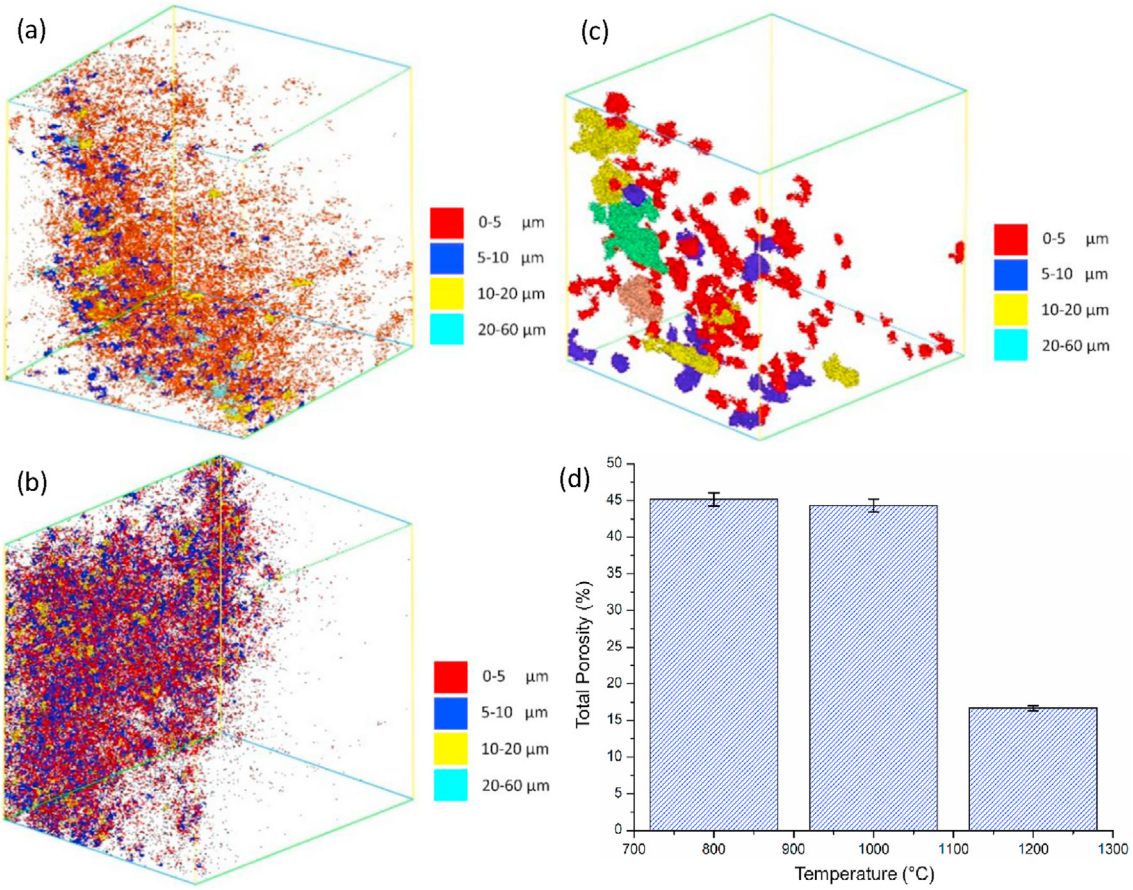

Fig. 4 – Various porosity size distribution at various heating temperatures (a) 800 °C, (b) 1000 °C, (c) 1200 °C and (d) total porosity of alkali activated slag.

maintained constant irrespective of mapping technique, and a step size of 1.5 um was applied. Analysis of acquired data was carried out using the Emax Evolution software and have been collected in Inorganic Crystal Structure Database (ICSD).

3. Result and discussion

3.1. *Microstructural observation*

Fig. 2 depicts the SEM images of the alkali activated slag heated at various temperatures (a) 800 °C, b) 1000 °C ,and c) 1200 °C. Pores appearance was observed in all heated alkali activated slag. By referring to Fig. 2a, it can be seen that the microstructure consists of abnormally grown large grains and small matrix grains with the presence of partial cracks on the periphery of the grains. The presence of the cracks would be cut across the grains to form a network as the heated temperature is increased. It can be noted that the microstructure consists of smaller grains as the temperature is increased up to 1000 °C.

The alkali activated slag heated at 1000 °C retains higher pores and grain growth as displayed in Fig. 2b. Thus, higher heated temperature can obviously promote grain growth and densification of alkali activated slag. A significant increase in densification surface was observed after heating at 1200 °C with high number of larger pores dominating the alkali activated slag matrix (Fig. 2c). The development of these pores indicated that the sintered necks started to grow, resulting in material densification. Additionally, the dense heated sample (Fig. 2c) displayed a shiny surface and formed a glassy phase during heating at 1200 °C which is the basis of a glaze.

The results of EDS revealed that the elemental composition of the crystalline grains (Point A and Point B) was consistent with that of gehlenite and anorthite grains, respectively. A similar result was also found by Liu et al. [35]. The phase development in the glassy phase suggested the crystallisation of anorthite at high temperature environment. Previous study by Han et al. [36] also described the crystallisation of anorthite phase was developed from the eutectic melt of gehlenite after heating up to 1200 °C. It can be concluded that the heating temperature of 1200 °C is quite sufficient for anorthite appearance to a major amount. The SEM and EDS results were in good agreement with the SXTM and EBSD results to be discussed in next section, whereby the pore and mineral phase formed are related to the microstructural evolution of alkali activated slag at high heating temperatures.

3.2. *Chemical bond analysis*

The IR spectra of alkali activated slag at various heating temperatures are presented in Fig. 3. The IR spectrum of alkali

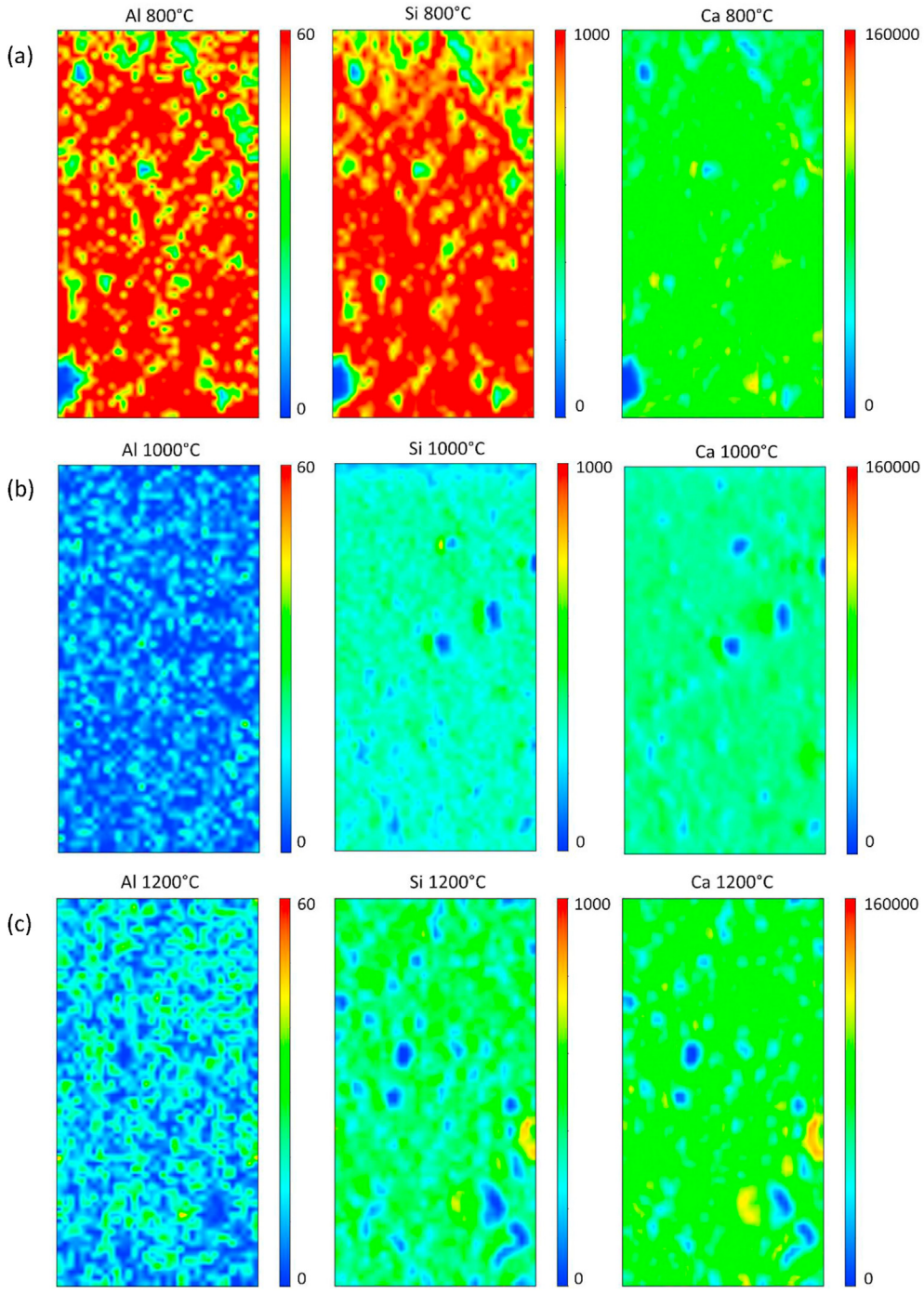

Fig. 5 – Micro-XRF elemental distribution maps of Ca–Al–Si in alkali activated slag at (a) 800 °C, (b) 1000 °C, and (c) 1200 °C heating temperatures.

Table 3 – Peak observation of alkali activated slag at various heating temperatures.

Heating temperature (°C)	Peaks (counts)		
	Ca-element	Si-element	Al-element
800	K-α (0.18×10^5)	K-α (0.22×10^3)	K-α (0.26×10^2)
1000	K-α (0.77×10^4)	K-α (0.69×10^2)	K-β (0.10×10^2)
1200	K-α (0.84×10^4)	K-α (0.82×10^2)	K-α (0.13×10^2)

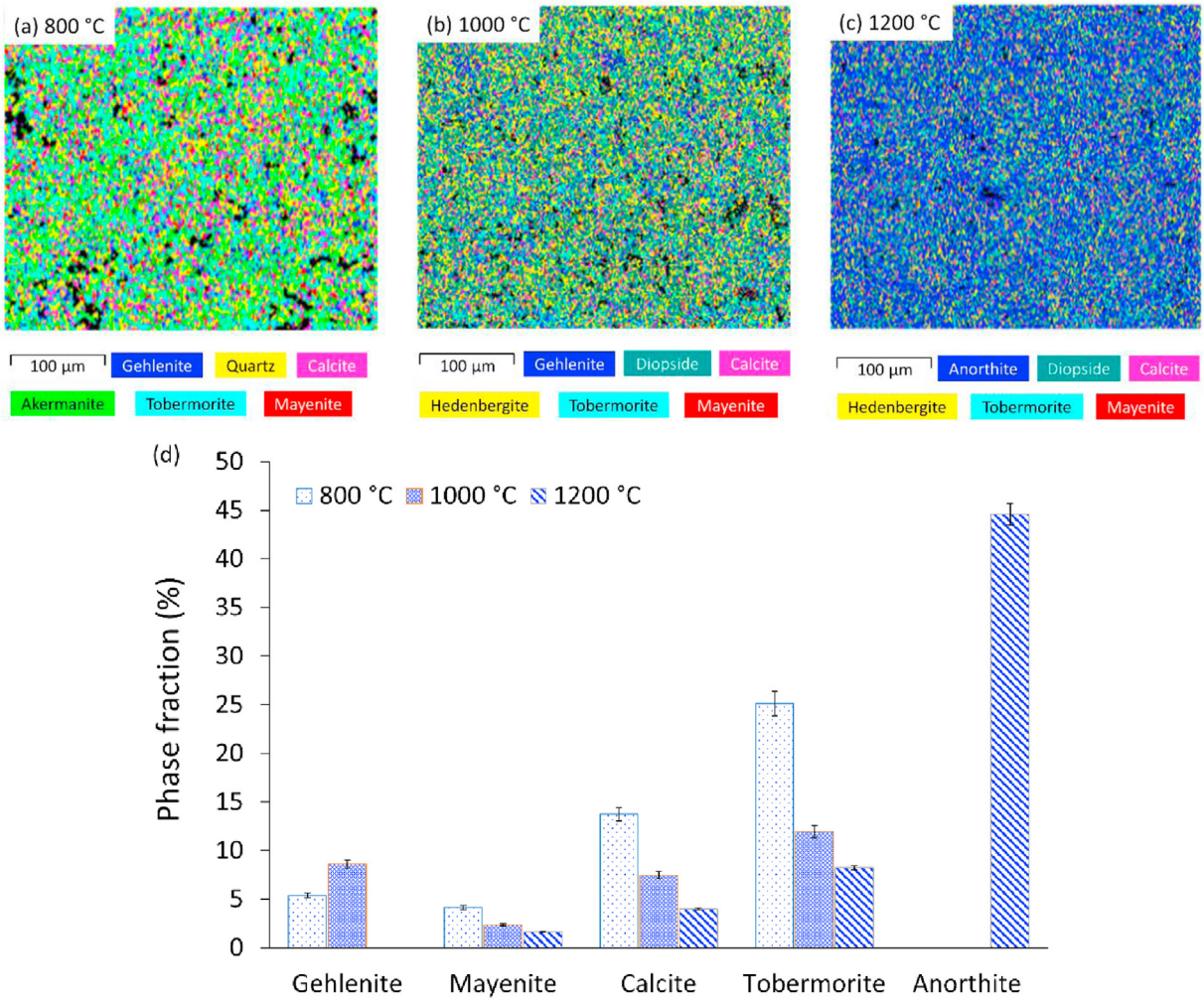

Fig. 6 – EBSD-mineral phase fraction on alkali activated slag at (a) 800 °C, (b)1000 °C, (c)1200 °C and (d) phase fraction of crystalline mineral formation.

activated slag illustrates the major absorption band at 900-910 cm^{-1} corresponding to the stretching vibrations of Si–O–Si/Al aluminosilicates and is an indicator of the alkali activated slag network formation [37]. The weak vibration modes at 3400-3800 cm^{-1} were in correspondence to OH-stretching vibration. The peak observed at 1430-1510 cm^{-1} was assigned to the formation of carbonate compound $(CO)_3^{2-}$. The transformation of spectral character with heating temperature occurred can be referred to Figs. 3a–c. It is evident that in the slight broadening of the spectral region of 810–910 cm^{-1} in samples heated at temperatures up to 1200 °C, in the same regions, the spectra contains band of gehlenite at 845-860 cm^{-1} [38]. The spectral region of 655–695 cm^{-1} in alkali activated slag becomes wider and shifts to higher wave number (693 cm^{-1}) at 1200 °C. Simultaneously, the spectral region of 1490–1510 cm^{-1} decreased as the heating temperature is increased due to the decomposition of calcite [39].

The small band at 850-860 cm^{-1} was corresponding to orthosilicate (SiO_4) compositions and attributed to symmetric stretching vibrations of silica tetrahedra with four non-bridging oxygen (NBOs) [40]. This wavenumber was disappeared after heated up to 1200 °C due to the connection of NBOs with Al–O and Si–O tetrahedral to form the crystalline anorthite. Presence of anorthite was also evident from the EDS spectroscopic result. The existence of the huge band at 910 cm^{-1} (Fig. 3c) is attributable to the strongest band of anorthite. It is also related to the Al–OH vibrations [41,42] and bridged with the vibrations of Si–O–Al which are formed by the linkages of $[SiO_4]^{4-}$ and $[AlO_4]^{5-}$ tetrahedra [43].

3.3. *Porosity evolution*

To further investigate the porosity evolution of the alkali activated slag at various heating temperatures, the synchrotron X-ray tomography (SXTM) technique was used. The advantage of SXTM technique is that it accurately evaluates the 3D pore structure of materials. Fig. 4 depicts the influence of heating temperature on pore network in the alkali activated slag samples. It can be seen that the overall porosity and pore size distribution depend on the heating temperature environment. Fig. 4a shows numerous pore structures in the size range of ~10 μm (45.2%) to the total porosity of alkali activated slag at 800 °C. Fig. 4b and 4c reveal the pore size distribution at

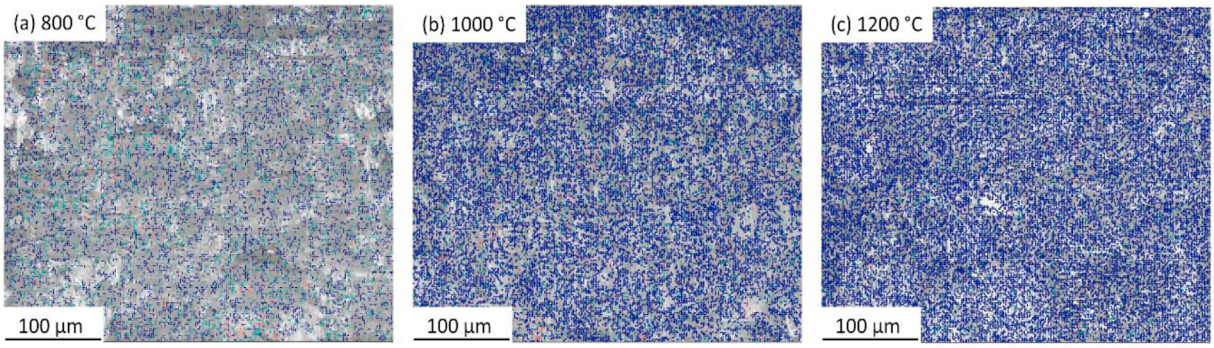

Fig. 7 – Grain boundaries images of alkali activated slag at (a) 800 °C, (b) 1000 °C, and (d) 1200 °C heating temperature.

higher range (~20 μm) and (~50 μm) after increasing the heating temperature at 1000 °C and 1200 °C, respectively. The frequency of pores distribution revealed that the quantity of smaller pores, especially in the range of ~20 μm is notably higher than the larger pores as increasing the heating temperature up to 1200 °C, the isolated pores (16.6%) in the range of ~20 μm are believed to contribute to the connected porosity while the larger pores are mostly noticed to be inter-granular pores due to the rapid growth of interparticle neck. This observation is similar with the results of surface morphology (Fig. 2).

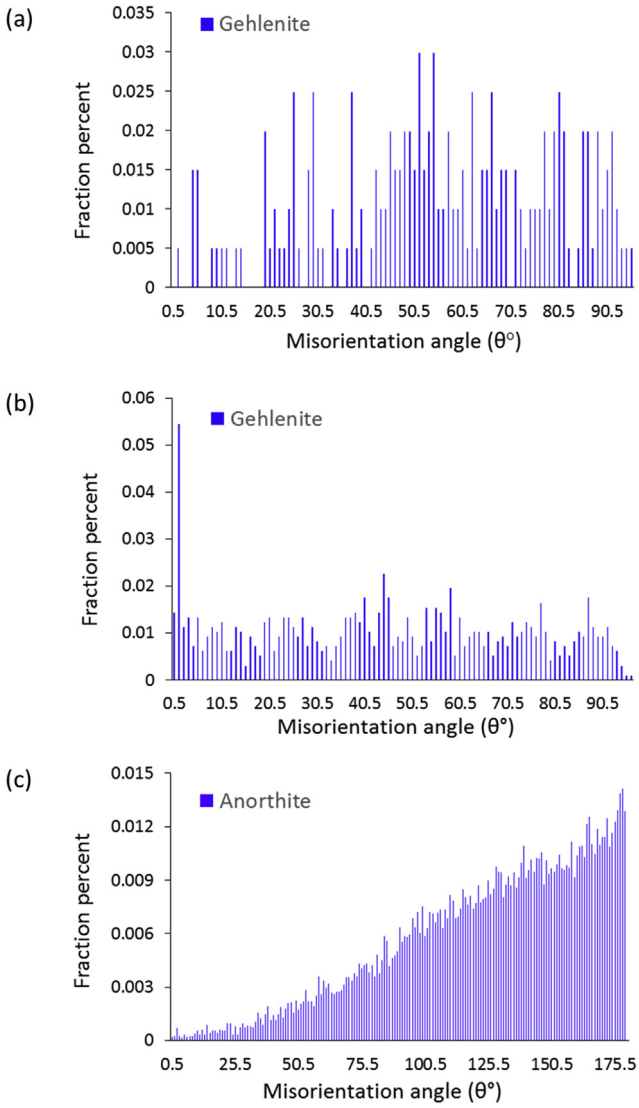

Fig. 8 – Misorientation angle distribution at (a) 800 °C, (b) 1000 °C and (c) 1200 °C heating temperatures.

Fig. 4d shows the reduction in total porosity of alkali activated slag after heated at higher temperature. The results provide an indication that porosity in alkali activated slag are unreachable after undergoing localised viscous sintering which forms isolated pores network, and accounts for the reduction in total porosity. Moreover, the reduction may also be influenced by the densification behavior as the denser surface is formed at 1200 °C heating temperature. Commonly, the densification process in alkali activated slag could be categorized into three stages. In the first stage, it will undergo particles packing and continue to the second stage which is described by the diffusion process consisting of the grain sliding and neck formation; lastly the third stage is related to pores destruction predominantly through grain boundaries [44]. Hence, a microstructure consisting of individual isolated pores formed at the grain boundaries could be observed as depicted in Fig. 2c.

3.4. *Elemental distribution*

In order to acquire an overview regarding the elemental distribution towards heating temperature, the alkali activated slag was further analysed via synchrotron micro-XRF mapping. Fig. 5 illustrates the localised area and the micro-XRF mapping in the alkali activated slag at 800 °C (Fig. 5a), 1000 °C (Fig. 5b) and 1200 °C (Fig. 5c), signifying that the main Si, Al and Ca are majorly located within the samples. Through the result obtained from the synchrotron micro-XRF, the elemental distribution, which reflected the minerals within the alkali activated structure can be located precisely. The distribution of Si with the combination of Al map allowed for the identification of the alkali activated slag backbone (Si–O–Al/Si). The colours blue, green and red represent low, medium and high intensities for each distribution element at the integrated area. High concentrated of Si region (Fig. 5a) indicates quartz grain. Based on the retrieved output, the Ca distribution was present in the boundary of the hydrated slag

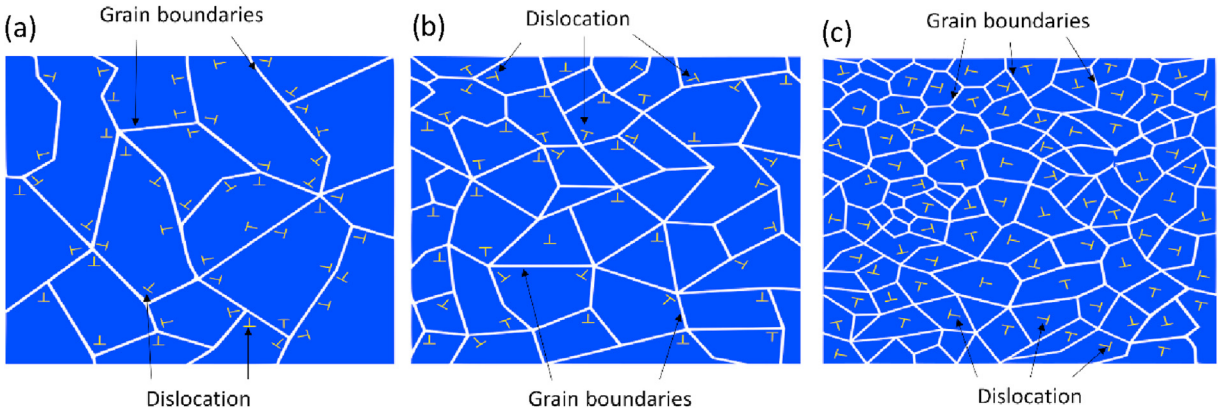

Fig. 9 – The dislocation activity within grain boundaries of alkali activated slag at (a) 800 °C, (b) 1000 °C and (c) 1200 °C.

mineral. The concentrated Ca region refers to the formation of calcite ($CaCO_3$) and the boundaries of tobermorite ($Ca_5Si_6O_{16}(OH)_2.4H_2O$) which is linked to the main structure.

The various heating temperatures resulted in significant changes on the Al and Ca elemental distribution, edging it towards to the formation of a stable crystalline phase. As depicted in Fig. 5, the transition intensity of alumina K-α (800 °C) to alumina K-β (1000 °C) was revealed, suggesting the substantial formation of gehlenite mineral at high-temperature crystallisation as tabulated in Table 3. At 1200 °C, it can be seen that Al and Ca are of high intensity in localised area, reflecting the formation of anorthite phase. This Ca-rich crystalline mineral is believed to be contributed to denser microstructure and glassy phase appearance, as portrayed in Fig. 2. Otherwise, the crystallisation of anorthite is promoted by the result of the calcination temperature. Increasing calcination temperature higher than 1100 °C will encourage the transition process of anorthite from gehlenite phase [45].

3.5. *Mineral phase formation*

The phase distribution of the alkali activated slag at various heating temperatures has been successfully described using an advanced technique of EBSD. The images of EBSD-phase distribution of alkali activated slag at (a) 800 °C, (b) 1000 °C and (c) 1200 °C are presented in Fig. 6.

Phase identification of individual mineral are presented in different colours at different heating temperatures. By referring to Fig. 6d, tobermorite (turquoise colour) dominated the samples surface of phase fraction at 800 °C (25.14%) and was reduced to the 8.24% after heated up to 1200 °C. The reduction of phase fraction is also displayed by calcite (pink colour) from 13.75% to 3.98% and mayenite (red colour) from 4.15% to 1.64%, respectively. The black spot indicates the pores formation during heating process and could contribute to further cracking due to the atmospheric water vapour absorption. The reduction of porosity also agreed with the finding in Section 3.3.

The phase distribution of gehlenite disappeared after being heated up to 1200 °C due to the lower thermodynamic stability characteristic. Meanwhile, a contradict observation was obtained using tobermorite, calcite and mayenite whereby these metastable mineral phases can withstand higher heating temperature. The relatively small equiaxed grain was observed with the whole phase distribution of alkali activated slag consisting of anorthite phase (blue colour) at 1200 °C as shown in Fig. 6c. The typical diopside, hedenbergite and anorthite were observed at higher heating temperature since these calcium-based minerals are commonly formed in the eutectic mixture [43]. It would be fruitful to correlate the grain structure with the phase distribution to develop the information about phase microstructure within the grain scale. Thus, the details of grain behavior correlating with crystallinity in the alkali activated slag at various heating temperatures will be discussed in the next section.

3.6. *Grain boundaries measurement*

Fig. 7 displays the grain boundary map of alkali activated slag at various heating temperatures. By referring to the grain boundary maps, the blue and grey lines represent the high angle grain boundaries, HAGB ($\theta > 15°$) and low angle grain boundaries, LAGB ($\theta = 2°\sim15°$), respectively. For the alkali activated slag at 800 °C, the high density LAGB can clearly be seen as shown in Fig. 7a. This can be explained by the occurrence of dislocation activity within the grains. Meanwhile, after the samples are heated at 1200 °C (Fig. 7c), the high density of HAGB was clearly observed which suggests the dynamic recrystallisation (DRX) during heating process. As heating temperature is increased, the enhanced density of the HAGB can be distinguished, and so does the LAGB.

The HAGB development can be attributed to the high heating temperature which increases the energy stored in the alkali activated slag, consequently contributing to the nucleation of the dynamically re-crystallised grains at the serrated HAGB [46]. It can also be seen that the density of the LAGB slightly decreased in the heated sample after being heated at 1200 °C, which could be due to the occurrence of the eutectic microstructure (Fig. 2c) from the transformation of LAGB to HAGB. The influence of heating temperatures on misorientation angle distribution is depicted in Fig. 8. Referring to the EBSD-phase mineral (Fig. 6), it can be visualized that gehlenite was fully crystallised into anorthite after being heated up to 1200 °C, which is a typical chemical reaction for anorthite crystallisation at higher temperature (Eq. (1)) [47]. In order to

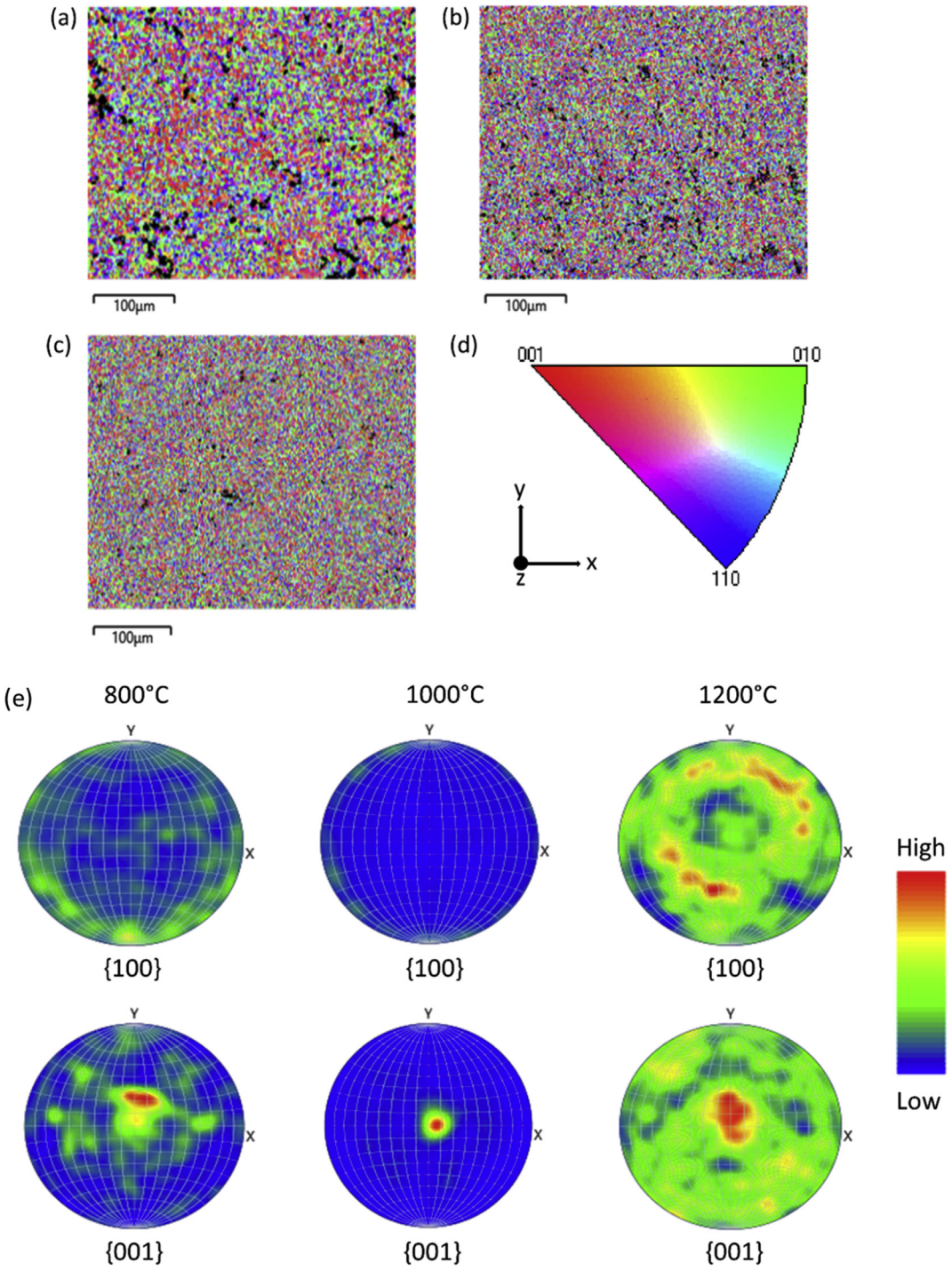

Fig. 10 – (a to c) Colored inverse pole figure (IPF) maps, (d) standard stereographic triangle and (e) pole figure of texture evolution on {001} and {100} planes in alkali activated slag.

understand the phenomenon, it is vital to consider the misorientation angle grain distribution between the minerals.

$$Ca_2Al_2SiO_7 \text{ (gehlenite)} + Al_2Si_2O_7 + SiO_2 \rightarrow 2CaAl_2Si_2O_8 \text{ (anorthite)} \quad (1)$$

LAGB and HAGB are dominant at heating temperature of 800 °C. The decrease of LAGB and HAGB after the heating temperature was higher is evident, due to increasing grain boundaries within the alkali activated slag (Fig. 7b) as related to the dislocation activity. However, some peak of LAGB appeared (<10°) for the sample heated at 1000 °C. It can be seen that at 50.5°–175.5°, there are peaks for the alkali activated slag samples heated at 1200 °C (Fig. 8c). Noticeably, the peaks obtained for anorthite mineral at 1200 °C are higher than gehlenite mineral heated below 1200 °C, which could be

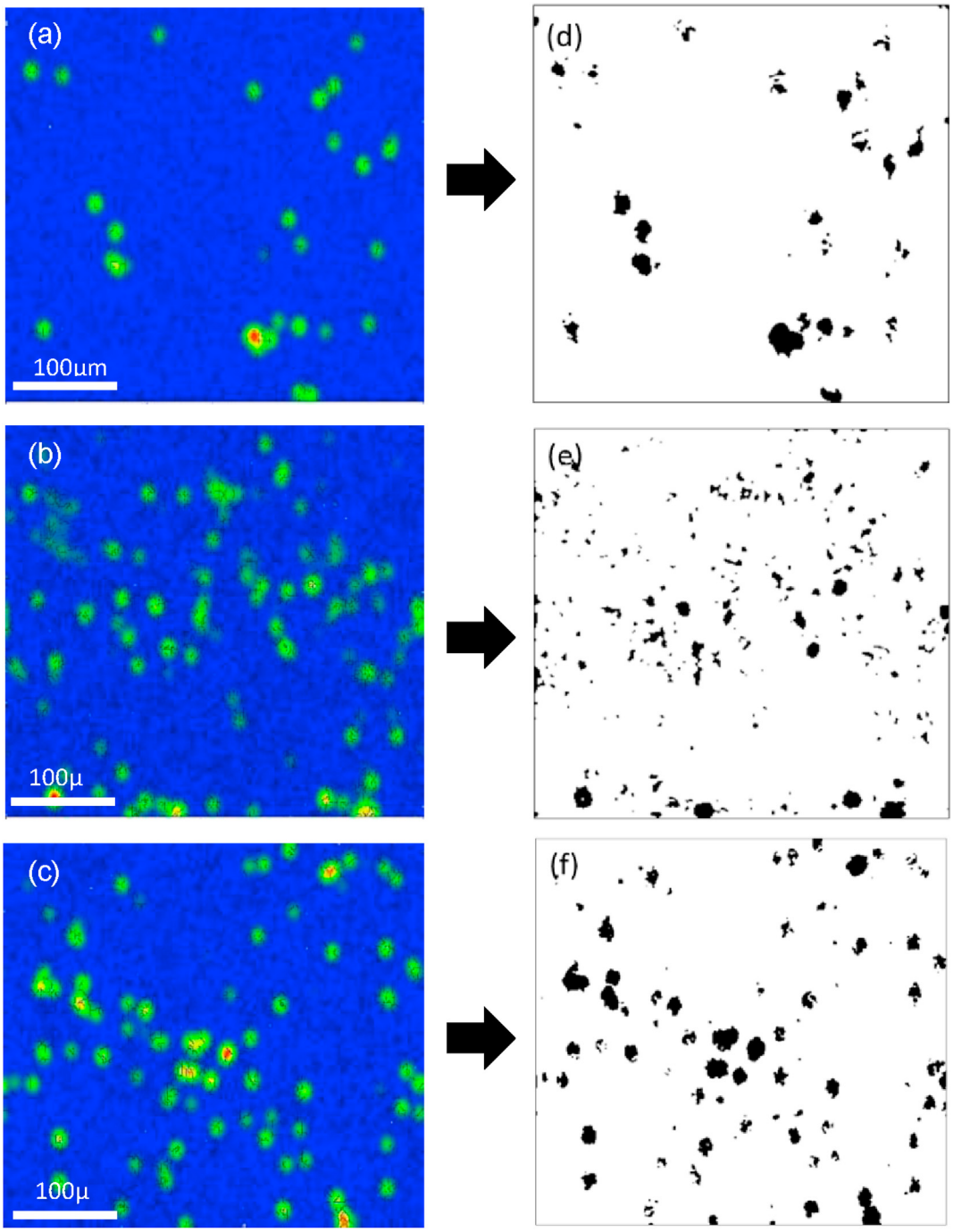

Fig. 11 – The strain contouring before and after threshold process on alkali activated slag at heating temperatures (a and d) 800 °C, (b and e)1000 °C and (c and f) 1200 °C.

due to the occurrence of dynamic recrystallisation (DRX) and eutectic microstructure surface during heating. This observation corroborates the ideas of Ma et al. [48] who suggested that anorthite is identified as eutectic at high temperature whereby it had readily reacted with quartz and other minerals to form a eutectic mixture. Also, Schoneveld et al. [49] speculated that the capacity of iron oxides and quartz play a role for the melting anorthite at high temperature.

The dislocation activity within the grains resulted from the heating effect on the alkali activated slag. This kind of defect simply moves throughout crystalline grains and develops in permanent distortion. As can be observed in Fig. 9, the microstructure displayed the grains development after the increase in heated temperature. The result of microstructure indicates that the appearance of fine grains is attributed to the limited dislocation movements within the crystal grains. The dislocation movement was stopped once a grain boundary has been reached. The dislocation "pile-up" at the grain boundaries and there is no direction for the dislocation movement. Hence, the formation of small grains has strengthened the

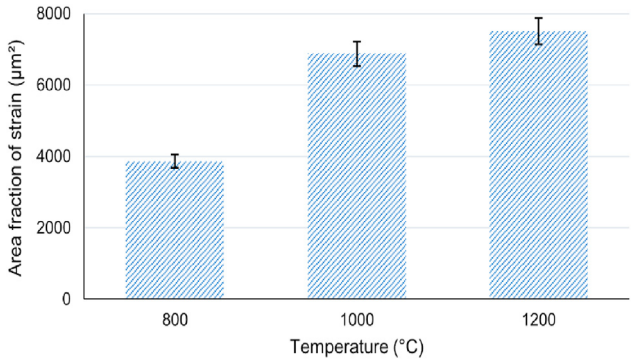

Fig. 12 – Area fraction of the strain on alkali activated slag at various heating temperatures.

material crystallinity [49]. The findings are consistent with Hesabi et al. [50] that stated that the finer the grain sizes of the crystal structure, the higher the mechanical properties of the material would be. This phenomenon is also known as grain-boundary strengthening or Hall-Petch strengthening [51].

3.7. *Crystal orientation and texture evolution*

Figs. 10a–10c display the colored inverse pole figure (IPF) map and the alkali activated slag at various heating temperatures. The color variation; red for {001}, green for {010} and blue for {110} as depicted in standard stereographic triangle (Fig. 10d), reflect the crystallographic orientation of each grain on the samples. Additionally, the color variation within the grain formation demonstrates variance in internal misorientations.

The appearance of more equiaxed microstructure and average grain size of ~10 μm can be obtained from samples heated at 1200 °C (Fig. 10c). As supported by the grain boundaries maps (Fig. 7c), it was confirmed that the grain boundaries within the equiaxed grains are HAGB ($\theta > 15°$), with major difference in misorientation. This huge misorientation is also reflected in the IPF maps whereby depicting substantial colour variation within the grain interior. Moreover, Fig. 10e displays the experimental pole figure recorded on {100} and {001} planes representing the texture of the alkali activated slag at various heating temperatures. The textures obtained on the samples at the same measurement areas were analysed for the IPF maps in Fig. 10a–10c.

As heated at 800 °C, the texture characteristic of the grains on alkali activated slag presented randomly {001} and {100} pole figures. As heating temperature is increased to 1000 °C, the {001} pole figure becomes weak while the {100} pole figure obtains an ideal preferred texture. This was believed due to the deformation of gehlenite grains with the reduction of LAGB and HAGB as supported by Fig. 8b. Nevertheless, the randomly oriented for {100} and preferred orientation for {001} pole figures are obtained after the samples are heated at 1200 °C. The textures present that the grain is preferentially oriented as suggested by the anorthite crystallisation.

3.8. *Strain localisation*

The area fraction of strain on the alkali activated slag at various heating temperatures had been quantitatively analysed as well as microstructural evolution has been conducted as shown in Fig. 11. The red color indicates a higher intensity of strain while blue represents a relatively lower strain. The higher heating temperature on the alkali activated slag was found to have significantly affected the strain appearance, as higher temperatures are known to have considerably increased the strain area fraction on the samples. It is observed that the strain distribution up to 1000 °C (Fig. 11b) is well distributed throughout the samples, indicating that a strain was developed during heating. In alkali activated slag at various heating temperatures, the heating exposure induced phase crystallisation is known as the main driver for microstructural evolution and grain boundaries transformation. As heating temperature is increased up to 1200 °C, an evolution of microstructural and higher strain distribution is expected. The changes could be due to the lower dislocation activity and thus, leading to higher storage of thermal strain in the alkali activated slag structure.

Strain contouring maps revealed that the localize highest strain intensity (red color) is about 5 μm. This is related to the variation of thermal strain in various grains boundaries depending on their crystallographic orientation. This was supported by the finding by Wang et al. [52], who posited that the higher number of grains boundaries resulted in the increase of fracture toughness and thermal tolerance for ceramic materials. Additionally, the qualitative measurement of strain can be related to the grain boundary misorientation. At 1200 °C, the higher fraction of HAGB (Fig. 8c) decreased the dislocation activity and thus developing the internal strain (higher stored energy). The area fraction of the strain on heated alkali activated slag showed a gradual increase from 3868.2 μm^2 to 7511.8 μm^2 following heated temperatures from 800 °C to 1200 °C as shown in Fig. 12, respectively.

4. Conclusion

The microstructure and porosity evolution of alkali activated slag at various heating temperatures were investigated experimentally in this paper. The effect of high heating temperature towards crystallography behavior and element distribution of alkali activated slag were examined. The microstructure analysis showed that there are increasing the densification surface and larger pores within the alkali activated slag matrix. The synchrotron micro X-ray tomography and synchrotron X-ray fluorescence reveal that the higher range (~50um) of pores distribution and intensity of localised Al elements were determined at 1200 °C.

The EBSD-phase distribution of the alkali activated slag showed that the crystalline phases of tobermorite, calcite and mayenite can withstand higher heating temperature. The grain boundaries analysis associated with crystal orientation confirm that the gehlenite was fully crystallised into anorthite. This is mainly due to the occurrence of dynamic recrystallisation and preferred orientation for {001} pole figure. Additionally, the crystallization of anorthite at 1200 °C results in higher equiaxed microstructure and high angle grain boundaries ($\theta > 15°$), which leads to the higher internal strain distribution. Hence, it was revealed that the alkali activated slag can withstand at high heating temperature up to 1200 °C.

This study highlights the development of alkali activated slag technology at high heating temperature, by using an advance techniques of synchrotron X-ray fluorescence, synchrotron X-ray tomography and electron backscatter diffraction.

Credit author statement

Ikmal Hakem Aziz : Conceptualization, Data curation, Investigation, Methodology, Writing-original draft and Writing-review & editing

Mohd Mustafa Al Bakri Abdullah : Project administration, Funding acquisition, Resources, Supervision, Validation and Visualization

M. A. A Mohd Salleh : Project administration, Funding acquisition, Resources, Supervision, Validation and Visualization

Sorachhon Yoriya : Investigation, Software and Data curation

Jitrin Chaiprapa : Investigation, Software and Data curation

Catleya Rojviriya: Investigation, Software and Data curation

Long Yuan Li : Validation and Visualization

Declaration of Competing Interest

The authors declare that they have no known competing financial interests or personal relationships that could have appeared to influence the work reported in this paper.

Acknowledgement

The authors gratefully acknowledge the Centre of Excellence Geopolymer and Green Technology (CEGeoGTech) and the School of Materials Engineering, UniMAP for their expertise and support. The authors wish to thank for the funding support obtained from the Fundamental Research Grant Scheme under the Malaysian Ministry of Education (MOE) and the support gained from "Partnership for Research in Geopolymer Concrete" in the framework of Marie Skłodowska-Curie RISE Grant Agreement (689857 H2020-MSCA-RISE-2015).

REFERENCES

[1] Bai Y, Collier N, Milestone N, Yang C. The potential for using slags activated with near neutral salts as immobilisation matrices for nuclear wastes containing reactive metals. J Nucl Mater 2011;413(3):183–92.

[2] Shojaei M, Behfarnia K, Mohebi R. Application of alkali-activated slag concrete in railway sleepers. Mater Des 2015;69:89–95.

[3] Türker HT, Balçikanli M, Durmuş İH, Özbay E, Erdemir M. Microstructural alteration of alkali activated slag mortars depend on exposed high temperature level. Construct Build Mater 2016;104:169–80.

[4] Davidovits J. Geopolymer cement a review. Technical Paper. In: Geopolymer science and technics, vol. 21. Saint-Quentin, France: Geopolymer Institute Library; 2013 January. p. 1–11. Geopolymer Institute Library.

[5] Gao X, Yu Q, Brouwers H. Reaction kinetics, gel character and strength of ambient temperature cured alkali activated slag–fly ash blends. Construct Build Mater 2015;80:105–15.

[6] Mobasher N, Bernal SA, Provis JL. Structural evolution of an alkali sulfate activated slag cement. J Nucl Mater 2016;468:97–104.

[7] Albidah A, Abadel A, Alrshoudi F, Altheeb A, Abbas H, Al-Salloum Y. Bond strength between concrete substrate and metakaolin geopolymer repair mortars at ambient and elevated temperatures. J Mater Res Technol 2020;9(5):10732–45.

[8] Özkal FM, Polat M, Yağan M, Öztürk MO. Mechanical properties and bond strength degradation of GFRP and steel rebars at elevated temperatures. Construct Build Mater 2018;184:45–57.

[9] Murri AN, Rickard W, Bignozzi M, Van Riessen A. High temperature behaviour of ambient cured alkali-activated materials based on ladle slag. Cement Concr Res 2013;43:51–61.

[10] Aziz IH, Abdullah MMAB, Heah C-Y, Liew Y-M. Behaviour changes of ground granulated blast furnace slag geopolymers at high temperature. Adv Cement Res 2019:1–11.

[11] Park SM, Jang JG, Lee N, Lee HK. Physicochemical properties of binder gel in alkali-activated fly ash/slag exposed to high temperatures. Cement Concr Res 2016;89:72–9.

[12] Rovnaník P, Bayer P, Rovnaníková P. Characterization of alkali activated slag paste after exposure to high temperatures. Construct Build Mater 2013;47:1479–87.

[13] Burciaga-Díaz O, Escalante-García JI. Comparative performance of alkali activated slag/metakaolin cement pastes exposed to high temperatures. Cement Concr Compos 2017;84:157–66.

[14] Rashad AM, Sadek DM, Hassan HA. An investigation on blast-furnace stag as fine aggregate in alkali-activated slag mortars subjected to elevated temperatures. J Clean Prod 2016;112:1086–96.

[15] Das S, Yang P, Singh SS, Mertens JC, Xiao X, Chawla N, et al. Effective properties of a fly ash geopolymer: synergistic application of X-ray synchrotron tomography, nanoindentation, and homogenization models. Cement Concr Res 2015;78:252–62.

[16] Duan P, Shui Z, Chen W, Shen C. Enhancing microstructure and durability of concrete from ground granulated blast furnace slag and metakaolin as cement replacement materials. J Mater Res Technol 2013;2(1):52–9.

[17] Igarashi S-i, Chen W, Brouwers H. Comparison of observed and simulated cement microstructure using spatial correlation functions. Cement Concr Compos 2009;31(9):637–46.

[18] Zhu X, Zhang Z, Yang K, Magee B, Wang Y, Yu L, et al. Characterisation of pore structure development of alkali-activated slag cement during early hydration using electrical responses. Cement Concr Compos 2018;89:139–49.

[19] Link T, Zabler S, Epishin A, Haibel A, Bansal M, Thibault X. Synchrotron tomography of porosity in single-crystal nickel-base superalloys. Mater Sci Eng A 2006;425(1–2):47–54.

[20] Wright SI, Nowell MM, Field DP. A review of strain analysis using electron backscatter diffraction. Microsc Microanal 2011;17(3):316–29.

[21] Xi L, Gu D, Guo S, Wang R, Ding K, Prashanth KG. Grain refinement in laser manufactured Al-based composites with TiB2 ceramic. J Mater Res Technol 2020;9(3):2611–22.

[22] Zhang B, Yin J, Zheng J, Liu X, Huang Z, Dusza J, et al. High temperature ablation behavior of pressureless sintered Ta0.8Hf0.2C-based ultra-high temperature ceramics. J Eur Ceram Soc 2020;40(4):1784–9.

[23] Tiamiyu A, Tari V, Szpunar J, Odeshi A, Khan A. Effects of grain refinement on the quasi-static compressive behavior of AISI 321 austenitic stainless steel: EBSD, TEM, and XRD studies. Int J Plast 2018;107:79–99.
[24] Bouaziz O, Allain S, Scott C, Cugy P, Barbier D. High manganese austenitic twinning induced plasticity steels: a review of the microstructure properties relationships. Curr Opin Solid State Mater Sci 2011;15(4):141–68.
[25] Salleh MM, Gourlay C, Xian J, Belyakov S, Yasuda H, McDonald S, et al. In situ imaging of microstructure formation in electronic interconnections. Sci Rep 2017;7:40010.
[26] Evans PG, Chen Y, Tilka JA, Babcock SE, Kuech TF. Crystallization of amorphous complex oxides: new geometries and new compositions via solid phase epitaxy. Curr Opin Solid State Mater Sci 2018;22(6):229–42.
[27] Mandal S, Bhaduri A, Sarma VS. A study on microstructural evolution and dynamic recrystallization during isothermal deformation of a Ti-modified austenitic stainless steel. Metall Mater Trans 2011;42(4):1062–72.
[28] Mirzadeh H, Cabrera J, Najafizadeh A, Calvillo P. EBSD study of a hot deformed austenitic stainless steel. Mater Sci Eng A 2012;538:236–45.
[29] Aziz IH, Abdullah MMAB, Salleh MM, Azimi EA, Chaiprapa J, Sandu AV. Strength development of solely ground granulated blast furnace slag geopolymers. Construct Build Mater 2020;250:118720.
[30] Ramli M, Salleh MM, Yasuda H, Chaiprapa J, Nogita K. The effect of Bi on the microstructure, electrical, wettability and mechanical properties of Sn-0.7 Cu-0.05 Ni alloys for high strength soldering. Mater Des 2020;186:108281.
[31] Solé V, Papillon E, Cotte M, Walter P, Susini J. A multiplatform code for the analysis of energy-dispersive X-ray fluorescence spectra. Spectrochim Acta, Part B 2007;62(1):63–8.
[32] Tiyasatkulkovit W, Promruk W, Rojviriya C, Pakawanit P, Chaimongkolnukul K, Kengkoom K, et al. Impairment of bone microstructure and upregulation of osteoclastogenic markers in spontaneously hypertensive rats. Sci Rep 2019;9(1):1–12.
[33] Kyrieleis A, Ibison M, Titarenko V, Withers PJ. Image stitching strategies for tomographic imaging of large objects at high resolution at synchrotron sources. Nucl Instrum Methods Phys Res Sect A Accel Spectrom Detect Assoc Equip 2009;607(3):677–84.
[34] Desrues J, Viggiani G, Besuelle P. Advances in X-ray tomography for geomaterials. John Wiley & Sons; 2010.
[35] Liu S, Qi C, Zhang S, Deng Y. Minerals in the ash and slag from oxygen-enriched underground coal gasification. Minerals 2016;6(2):27.
[36] Han Y, Li C, Bian C, Li S, Wang C-A. Porous anorthite ceramics with ultra-low thermal conductivity. J Eur Ceram Soc 2013;33(13–14):2573–8.
[37] Choi YC, Park B. Effects of high-temperature exposure on fractal dimension of fly-ash-based geopolymer composites. J Mater Res Technol 2020;9(4):7655–68.
[38] Akyuz S, Akyuz T, Basaran S, Bolcal C, Gulec A. Analysis of ancient potteries using FT-IR, micro-Raman and EDXRF spectrometry. Vib Spectrosc 2008;48(2):276–80.
[39] Hager I. Behaviour of cement concrete at high temperature. Bull Pol Acad Sci Tech Sci 2013;61(1):145–54.
[40] Böke N, Birch GD, Nyale SM, Petrik LF. New synthesis method for the production of coal fly ash-based foamed geopolymers. Construct Build Mater 2015;75:189–99.
[41] Harabi A, Zaiou S, Guechi A, Foughali L, Harabi E, Karboua N-E, et al. Mechanical properties of anorthite based ceramics prepared from kaolin DD2 and calcite. Cerâmica 2017;63(367):311–7.
[42] Sahnoun RD, Bouaziz J. Sintering characteristics of kaolin in the presence of phosphoric acid binder. Ceram Int 2012;38(1):1–7.
[43] Perná I, Šupová M, Hanzlíček T. Gehlenite and anorthite formation from fluid fly ash. J Mol Struct 2018;1157:476–81.
[44] Wang S, Zhang J, Luo D, Gu F, Tang D, Dong Z, et al. Transparent ceramics: processing, materials and applications. Prog Solid State Chem 2013;41(1–2):20–54.
[45] Zhang D, Hu S, Sun H, Zhang W, Wang B. Mineral transition of high-temperature sintering confirmed in $CaAl_2O_4$-Ca_2SiO_4 non-equilibrium binary system. Construct Build Mater 2020;234:117402.
[46] Liu Z, Li P, Xiong L, Liu T, He L. High-temperature tensile deformation behavior and microstructure evolution of Ti55 titanium alloy. Mater Sci Eng A 2017;680:259–69.
[47] Ptáček P, Opravil T, Šoukal F, Havlica J, Holešinský R. Kinetics and mechanism of formation of gehlenite, Al–Si spinel and anorthite from the mixture of kaolinite and calcite. Solid State Sci 2013;26:53–8.
[48] Uda M, Gopinath SC, Hasfalina C, Faridah S, Bunawan S, Sabrina WN, et al. Production and purification of antibody by immunizing rabbit with rice tungro bacilliform and rice tungro spherical viruses. Process Biochem 2018;68:37–42.
[49] Schoneveld L, O'Neill HSC. The influence of melt composition on the partitioning of trace elements between anorthite and silicate melt. Contrib Mineral Petrol 2019;174(2):13.
[50] Hesabi ZR, Haghighatzadeh M, Mazaheri M, Galusek D, Sadrnezhaad S. Suppression of grain growth in sub-micrometer alumina via two-step sintering method. J Eur Ceram Soc 2009;29(8):1371–7.
[51] Tejedor R, Edalati K, Benito JA, Horita Z, Cabrera JM. High-pressure torsion of iron with various purity levels and validation of Hall-Petch strengthening mechanism. Mater Sci Eng A 2019;743:597–605.
[52] Wang J, Chong X, Zhou R, Feng J. Microstructure and thermal properties of RETaO4 (RE= Nd, Eu, Gd, Dy, Er, Yb, Lu) as promising thermal barrier coating materials. Scripta Mater 2017;126:24–8.